RSC Advances

PAPER

View Article Online
View Journal | View Issue

Cite this: *RSC Adv.*, 2026, **16**, 15152

O/N-carbon dots as a fluorescent nanoprobe for sensitive COX-2 inhibitor detection: comprehensive validation and application to pharmacokinetic studies in rats with acute liver injury

Doaa H. Rushdy, *[a] Al-Montaser Bellah H. Ali,[b] Wesam M. El-Koussi[a] and Noha N. Atia[b]

Etoricoxib (ETX), a widely used selective cyclooxygenase-2 (COX-2) inhibitor, currently does not have a direct spectrofluorometric method suitable for regular bioanalytical measurement. This investigation introduces an innovative spectrofluorometric approach for the determination of ETX, based on orange-emitting oxygen/nitrogen-doped carbon dots (O/N-CDs). The approach relies on a turn-off mechanism where ETX causes concentration-dependent fluorescence quenching of O/N-CDs, primarily through the inner filter effect, further supported by dynamic quenching. The assay demonstrated remarkable linearity across the range of 50–1000 ng mL^{-1}, with a limit of detection developed at 15.80 ng mL^{-1}. Spiked plasma yielded recovery values that ranged from 94.52% to 96.01%. Protein precipitation followed by reversed-phase C_{18} solid-phase extraction was employed to ensure method selectivity. The clinical significance was demonstrated by the successful implementation in rat plasma pharmacokinetic studies, which included both healthy subjects and those with thioacetamide-induced acute liver injury. The method effectively quantified ETX and identified notable pharmacokinetic variations between the groups. Furthermore, the evaluation of greenness through the multi-color assessment tool and analytical green star area validated the method's positive environmental attributes. This fluorescence-based assay offers a practical, sensitive, and environmentally friendly alternative to traditional chromatographic methods for ETX quantification, facilitating routine bioanalysis, and pharmacokinetic studies.

Received 18th January 2026
Accepted 1st March 2026

DOI: 10.1039/d6ra00452k

rsc.li/rsc-advances

1. Introduction

Chronic pain and inflammation have a substantial impact on quality of life, functioning, and socioeconomic productivity, and they are major contributors to the worldwide illness burden.[1,2] Rheumatoid arthritis and osteoarthritis are progressive, long-term inflammatory diseases that need ongoing medication to control pain, preserve joint function, and prevent or postpone disability.[3] In order to maintain analgesic efficacy while reducing upper gastrointestinal toxicity, clinical practice has gradually shifted from traditional non-selective nonsteroidal anti-inflammatory medicines (NSAIDs) to selective cyclooxygenase-2 (COX-2) inhibitors.[4,5] Osteoarthritis, rheumatoid arthritis, ankylosing spondylitis, and certain acute painful diseases are all treated with etoricoxib (ETX), a selective COX-2 inhibitor.[6] The dose of ETX is determined by the indication and is given once daily: 30–60 mg for osteoarthritis, 90 mg for osteoarthritis and rheumatoid arthritis/ankylosing spondylitis, and 120 mg for acute gout or dysmenorrhea.[7] Although side effects such as headache, dizziness, dyspepsia, nausea, peripheral edema, and dose-dependent increases in blood pressure and liver enzyme levels are commonly reported, ETX is generally well tolerated.[7]

ETX is nearly entirely absorbed upon oral administration, exhibiting an oral bioavailability approaching 100% in healthy subjects.[8] A majority of the medication in the bloodstream is bound to proteins (about 92%), with peak plasma concentrations often attained within 1 to 2 h.[8] The terminal half-life in humans is around 22 h, which justifies once-daily administration.[8] Hepatic clearance is the primary elimination route, as evidenced by the drug's significant hepatic biotransformation through cytochrome P450-mediated oxidative pathways and the percentage excreted unchanged in urine being less than 1%.[9] Due to ETX's significant reliance on hepatic metabolism for systemic clearance, any decrease in hepatic functional capacity is anticipated to modify its pharmacokinetic profile and increase the risk of increased exposure.[9] So, comprehensive

[a]*Department of Pharmaceutical Analytical Chemistry, Faculty of Pharmacy, Sohag University, Sohag 82524, Egypt. E-mail: doaa.hassan@pharm.sohag.edu.eg*
[b]*Department of Pharmaceutical Analytical Chemistry, Faculty of Pharmacy, Assiut University, Assiut 71515, Egypt*

bioanalytical assessment is particularly important in cases of hepatic impairment, given that the pharmacokinetics of ETX in liver dysfunction are insufficiently defined.

Although several analytical methods have been proposed for determining ETX, each has drawbacks. Although high-performance liquid chromatography (HPLC) methods[10–17] provide exceptional sensitivity and selectivity, they necessitate expensive equipment, lengthy analysis times, and labor-intensive sample preparation. High-performance thin-layer chromatography (HPTLC) techniques[18,19] show insufficient sensitivity and repeatability in plasma applications. The limitations of ultraviolet-visible (UV-vis) spectrophotometric systems[20–23] include their dependence on potentially harmful chemical solvents and spectrum interferences. Although capillary electrophoresis methods[24] offer quick separations, they are limited by the necessity for maintenance and the μg mL^{-1} range of detection. Despite ETX's widespread clinical use as a selective COX-2 inhibitor, as far as we are aware, no spectrofluorometric method for measuring it has been published. Compared to other chromatographic techniques, spectrofluorometry offers great sensitivity, convenience of use, and requires less sample preparation, making this analytical gap particularly noteworthy. The development of a validated spectrofluorometric method for ETX would provide a viable substitute for routine therapeutic medication monitoring, enabling rapid, economical, and eco-friendly quantification while guaranteeing robust analytical performance.

Carbon dots (CDs) have emerged as significant fluorescent nanoprobes for pharmaceutical detection in biological systems, offering clear advantages over traditional analytical methods.[25] Carbon-based nanomaterials, generally under 10 nm in diameter, exhibit remarkable fluorescent, chemical, and mechanical characteristics. Their exceptional biocompatibility, distinctive optical properties, affordability, and commitment to environmental sustainability are widely acknowledged.[26] Carbon dots improve biological sensing through the detection and quantification of analyte concentrations based on their photoluminescence properties.[27] Recent uses of nitrogen-rich carbon dots (N-CDs) illustrate how quickly they can be used as effective fluorescent probes for drug detection in biological matrices. N-CDs sensor for finding the JAK-inhibitor abrocitinib in human plasma.[28] Natural-precursor N-CDs derived from guava fruit have been utilized for the spectrofluorometric measurement of the antipsychotic risperidone in human plasma.[29] Carbon dots are very flexible and can find compounds in a wide range of biological matrices, such as blood, urine, saliva, tears, and other liquid tissues that are easy to collect. This quality makes them perfect for therapeutic drug monitoring, where quick, easy, and cheap ways to find drugs are needed for routine clinical use.[30–33]

o-Phenylenediamine (OPD) has been employed in conjunction with *N*,*N*-dimethylformamide (DMF) to synthesize highly fluorescent CDs. Yang *et al.* developed a hydrothermal method employing OPD as the carbon source and DMF as the solvent to synthesize functionalized carbon quantum dots (CQDs-OPD), which were later utilized as a ratiometric fluorescence probe for the selective and sensitive detection of Cu^{2+}.[34] The CQDs-OPD probe demonstrated a dual-emission response to Cu^{2+} and was effectively employed for the quantification of Cu^{2+} in real water samples.[34] OPD/DMF CDs has been employed to develop N-CDs for metal-ion sensing; however, its use has not been extended to the quantitative analysis of small-molecule drugs in biological fluids.

This research presents an innovative spectrofluorometric method for the detection of ETX using orange-emitting CDs (OCDs). The primary precursors (OPD and DMF) utilized in Yang's Cu^{2+} probe are subjected to different solvothermal conditions to generate OCDs, which are designed as a fluorescent nanoprobe for ETX detection. This innovation arises from the application of the inner filter effect mechanism, wherein the UV absorption properties of ETX correspond with the excitation spectrum of OCDs. This results in concentration-dependent fluorescence quenching, facilitating direct, label-free quantification without requiring complex derivatization or extensive sample preparation. This approach differs from traditional methods that require expensive equipment and specialized analytical expertise. This approach utilizes the unique optical characteristics of OCDs, operating in a spectral range that minimizes interference from biological matrices, thus enhancing signal-to-noise ratios relative to conventional blue or green-emitting fluorescent probes. The method demonstrates significant clinical relevance through its successful application to actual rat plasma samples, enabling accurate determination of pharmacokinetic parameters in healthy and hepatic rats' plasma and thereby affirming its utility in pharmacokinetics. The proposed approach represents an important step towards developing readily available and inexpensive analytical methods for ETX monitoring.

The proposed method combines protein precipitation with reversed-phase C_{18} solid-phase extraction[35] to reduce matrix effects and remove plasma interferences while limiting organic solvent consumption and maintaining the advantages of an essentially aqueous procedure. The assay was applied to a full pharmacokinetic study in rats, confirming suitability for real biological samples and enabling comparison between healthy animals and thioacetamide-induced acute liver injury (TAA induced ALI), thereby linking the method to disease-state evaluation. Environmental performance was assessed using the multi-color assessment (MA)[36] framework together with the analytical green star area (AGSA),[37] demonstrating a favorable balance between sustainability, analytical performance, and practical feasibility. Compared with the previously reported OPD/DMF-derived carbon-dot probe, which was limited to Cu^{2+} detection in simple water matrices and lacked *in vivo* application, the present O/N-CD assay is validated for plasma analysis, provides high recovery and precision in protein-rich samples, and includes a documented greenness profile relevant to routine bioanalysis and pharmacokinetic studies.

2. Experimental

2.1. Materials and reagents

Etoricoxib (ETX, 99.5% purity) was supplied by EVA Pharma (Cairo, Egypt). *o*-Phenylenediamine (OPD) and anhydrous *N*,*N*-dimethylformamide (DMF) were obtained from Sigma-Aldrich

(Steinheim, Germany). Quinine sulfate was purchased from Alfa Aesar (Ward Hill, MA, USA). Anselacox® tablets (120 mg ETX/tablet) were obtained from a local pharmacy. Phosphoric acid (H_3PO_4), boric acid (H_3BO_3), acetic acid (CH_3COOH), and sodium hydroxide (NaOH) were purchased from El-Nasr company for intermediate chemicals (Cairo, Egypt). D-Glucose, L-ascorbic acid and uric acid and analytical grade salts as potassium chloride (KCl), calcium chloride ($CaCl_2$) and sodium chloride (NaCl) were purchased from Merck (Darmstadt, Germany). Ibuprofen, paracetamol, prednisone, amlodipine besylate and ranitidine HCl were obtained from Sigma-Aldrich (Steinheim, Germany). Thioacetamide from Sigma-Aldrich (Steinheim, Germany). Kits for activity assays of alanine aminotransferase (ALT), aspartate aminotransferase (AST) and total bilirubin were purchased from (Biodiagnostic Company, Egypt). Ultra-pure water (resistivity > 18 MΩ cm) was used in all experiments. All reagents were of analytical grade and used without further treatment. The Britton–Robinson buffer was prepared as a mixture of 0.2 M phosphoric acid, 0.2 M boric acid, and 0.2 M glacial acetic acid, adjusted to the desired pH using 0.2 M NaOH.

2.2. Instrumentation

UV-visible absorption spectra were obtained using a Shimadzu UV-1601 spectrophotometer (Japan) equipped with a 1 cm quartz cell. Fluorescence emission spectra were recorded on a Shimadzu RF-5301PC spectrofluorometer (Tokyo, Japan) with a slit width of 5 nm. O/N-CDs were characterized by Nicolet 6700 FT-IR spectrophotometer (Thermo Electron Corporation, USA) in the range of 400–4000 cm^{-1}. The XRD pattern of O/N-CDs was recorded on a Philips PW 1700 X-ray diffractometer (Eindhoven, Netherlands). A JEM-1400 Flash TEM from JEOL (Tokyo, Japan). Surface functional groups of O/N-CDs were characterized by X-ray photoelectron spectrometer (XPS, ESCA Ulvac-PHI 1600, PHI Quantum 2000 XPS system, Physical Electronics, USA), and Milli-Q water purification system (Thermo scientific Barnstead Smart 2 Pure 3 UV, Hungary).

2.3. Preparation of O/N-CDs

In a typical synthesis, 0.2 g of OPD was dissolved in 10.0 mL of DMF to give a clear solution, which was then transferred to a 50 mL Teflon-lined autoclave. The sealed vessel was heated at 200 °C for 9 h. After it cooled to room temperature on its own, a deep yellow solution was obtained. The mixture was filtered through a 0.22 μm membrane to remove any insoluble residues, and the crude product was redispersed in water. This dispersion was purified by dialysis against deionized water for 2 days using a 1000 Da molecular-weight-cutoff bag. The purified solution was finally lyophilized to yield the O/N-CDs.

2.4. Quantum yield

SI material contains full information about the experimental approach.

2.5. Method of analysis

For each measurement, 1.2 mL of the O/N-CD dispersion (12.0 μg mL^{-1}) was mixed with 1.0 mL of ETX solution prepared at the desired concentration. The mixture was left to equilibrate for 1.0 min, then Britton–Robinson buffer (pH 8.0) was added to bring the total volume to 5.0 mL. Fluorescence spectra were recorded using 270 nm as the excitation wavelength and monitoring the emission at 580 nm. All fluorescence measurements were performed in triplicate ($n = 3$) under identical conditions, and the average values were used for data analysis.

2.6. Animals

The Animal Research Facility at Assiut University provided the adult Sprague-Dawley rats (body weight 290 ± 15 g, $n = 16$), which were kept in conventional polycarbonate cages with a 12 h light/dark cycle, an ambient temperature of 22 ± 2 °C, and a relative humidity of 50–60%. Throughout the investigation, the animals were provided with free access to filtered tap water and regular laboratory feed. Prior to any experimental modification, rats were given a 7-day acclimation period. Following acclimation, they were split into two experimental groups ($n = 8$ per group) at random: a healthy control group and a thioacetamide (TAA) induced hepatic impaired group. The latter was developed using earlier findings, where rats were administered 300 mg kg^{-1} of TAA for two days in a row.[38,39] To put it briefly, 100 mg mL^{-1} of TAA was dissolved in 0.9% normal saline. For two consecutive days, separated by 24 h, the hepatic impaired rats got intraperitoneal injections of 300 mg kg^{-1} of TAA, while the rats in the control group received an equivalent volume of normal saline. Aspartate aminotransferase (AST), alanine aminotransferase (ALT) and total bilirubin in serum using common kits were evaluated to confirm the dysfunction of the liver. Every rat was fed a typical diet. Rats' drinking water was supplemented with 3% glucose, 0.3% sodium chloride, and 0.149% potassium chloride to prevent hypoglycemia and electrolyte imbalance, which can happen after modeling. The animals were ready for the subsequent tests 24 h after the second dose. Any indications of illness or suffering were noted and handled in accordance with institutional guidelines for animal care. The Institutional Animal Ethics Committee of the Faculty of Veterinary Medicine at Assiut University authorized all experimental techniques in accordance with the Guidelines for the Care and Use of Laboratory Animals (Approval number 06/2025/0358).

2.7. Steps for collecting, preparing, and extracting samples

Prior to pharmacokinetic dosing, both control and TAA-treated rats were fasted overnight (water ad libitum) after hepatic damage was confirmed. ETX was given as a single oral dose of 12.33 mg kg^{-1} by gastric gavage after being dissolved in regular saline. This dose is within the range utilized in earlier preclinical ETX pharmacokinetic studies and was chosen by allometric conversion from the usual human therapeutic dose.[40] Rats' tail veins were used to obtain serial blood samples (~0.3 mL) before the treatment and at 0.25, 0.5, 1.0, 1.5, 2, 3, 4, 8, 16, and 24 h

after the dose. After being promptly moved to heparinized microtubes, the samples were centrifuged for 10 minutes at 4 °C at 10 000 rpm. After being separated, plasma was aliquoted into micro vials that were shielded from light and kept at −20 °C until analysis. 250 μL of thawed plasma was put into 1.5 mL Eppendorf tubes for bioanalysis, and it was diluted with 250 μL of methanol. SPE was applied to the supernatant after it had been centrifuged for 10 minutes at 10 000 rpm and put onto Cleanert™ ODS C_{18} cartridges (30 mg, 1.0 mL). Following the conditioning of the cartridges with 2.0 mL of methanol and 2.0 mL of water. After loading the prepared samples onto the cartridges, any interferences were eliminated by washing them with 1.0 mL of 10% methanol and 1.0 mL of water. After that, methanol was used to elute ETX, and the collected eluates were examined using the method outlined in Section 2.5. The same process was applied to drug-free blank plasma samples, which were used as negative controls in the analysis.

2.8. Pharmacokinetic study

A noncompartmental analysis framework in PKSolver (Excel add-in, v2.0)[41] was used to examine the plasma concentration–time profiles of ETX after a single oral dosage in rats with both TAA-induced acute liver damage (ALI) and normal hepatic function (Control). The elimination half-life ($t_{1/2} = 0.693/K_{el}$) was derived from the terminal elimination rate constant (K_{el}), which was derived from the log-linear terminal phase by linear regression of the natural logarithm of plasma concentration *vs.* time. C_{max} (observed maximum plasma concentration), T_{max} (time to reach C_{max}), AUC_{0-t} (area under the plasma concentration–time curve from time zero to the last quantifiable concentration, using the linear trapezoidal rule), $AUC_{0-\infty}$, $AUMC_{0-\infty}$, mean residence time (MRT = AUMC/AUC), apparent oral clearance ($CL/F = Dose/AUC_{0-\infty}$), and apparent volume of distribution ($Vd/F = (CL/F)/K_{el}$) were the noncompartmental parameters that were calculated. For each group ($n = 8$), pharmacokinetic parameters are represented as mean ± SD. GraphPad Prism 9 was used to compare the normal and ALI groups using two-tailed unpaired *t*-tests.

3. Results and discussion

3.1. Morphological and structural characterization

The size distribution and surface morphology of the produced O/N-CDs were examined using transmission electron microscopy (TEM). The nanoparticles exhibited an average diameter of 3.4 nm and displayed a nearly spherical morphology, as illustrated in Fig. 1A. The size-distribution histogram (Fig. 1A) further indicates a homogeneous dispersion of the particles. High-resolution TEM (HRTEM) imaging revealed clearly defined lattice fringes with an interplanar spacing of 0.23 nm (inset, Fig. 1A), corresponding to the (100) crystallographic planes of the graphite phase.[42]

The X-ray diffraction (XRD) pattern of the O/N-CDs (Fig. 1B) is dominated by a broad, weak hump centered at about $2\theta = 21.8^{\circ}$, which is characteristic of largely amorphous carbon with only short-range turbostratic order. No distinct, well-defined Bragg peaks are present, indicating that extended crystalline domains are essentially absent. A few thin, narrow peaks riding on the diffuse halo at higher angles are attributed to minor residual crystallites or background contributions.[43]

The Fourier-transform infrared spectroscopy (FT-IR) spectrum of the O/N-CDs (Fig. 1C) indicates a chemically rich surface, showing both preservation of aromatic fragments from the starting material and effective introduction of oxygen- and nitrogen-containing functionalities. A broad band centered at 3406 cm^{-1} is assigned to overlapping O–H and N–H stretching, consistent with surface hydroxyl groups and residual primary/secondary amines originating from the OPD precursor. Two bands at 3053 and 2786 cm^{-1} correspond to aromatic and aliphatic C–H stretching, respectively, suggesting the coexistence of aromatic domains with newly formed sp^3 carbon sites within the carbon-dot framework.[44] A prominent absorption at 1669 cm^{-1} is attributed to vibrations of conjugated C=C/C=N together with amide-like C=O stretching, supporting condensation reactions and partial carbonization during formation. The peak at 1399 cm^{-1}, associated with C–N stretching and N–H bending, further confirms the presence of nitrogen functionalities. Signals observed at 1241 and 1171 cm^{-1} are assigned to C–O stretching (phenolic/alcoholic groups) and C–N stretching of aromatic amines, indicating oxidation and surface functionalization during synthesis.[44] In addition, bands at 931, 740, and 620 cm^{-1} arise from out-of-plane aromatic C–H bending, consistent with retained benzene-ring structures from the precursor. Overall, these bands confirm that the CDs carry hydroxyl and other oxygenated groups while preserving key aromatic and nitrogen-rich structural motifs.[45]

Survey X-ray photoelectron spectroscopy (XPS) of the O/N-CDs (Fig. 1D) shows that the particle surface is dominated by carbon, with smaller but clear amounts of nitrogen and oxygen. The C 1s signal between 280 and 296 eV accounts for 65.3% of the atoms detected, while the N 1s and O 1s regions (392–410 and 525–545 eV) contribute 25.1% and 9.6%, respectively. The relatively low oxygen content points to only mild oxidation during the solvothermal step, whereas the high nitrogen content reflects efficient transfer of nitrogen from the OPD precursor. Fitting of the high-resolution C 1s spectrum (Fig. S1A) reveals a main peak at 284.4 eV arising from sp^2 C=C/C–C in graphitic or aromatic domains, and a second component at 285.9 eV assigned to C–N and C=N, consistent with carbon–nitrogen linkages formed through condensation and cyclization during heating. A shoulder at 287.7 eV is associated with C=O groups generated by surface oxidation.[43] The N 1s spectrum (Fig. S1B) contains two distinct contributions: a peak at 398.0 eV characteristic of pyridinic nitrogen located in aromatic rings at edge or defect sites, and a peak at 399.6 eV attributed to amino nitrogen (–NH_2/–NH–), either preserved from the starting material or produced by partial oxidation and rearrangement during synthesis.[44] The O 1s region (Fig. S1C) is mainly made up of a component at 531.6 eV from C=O in carbonyl, quinone, or carboxyl groups and another at 532.0 eV from C–O in hydroxyl, ether, or phenolic groups. These oxygen-containing groups enhance hydrogen bonding and keep the dots well dispersed in

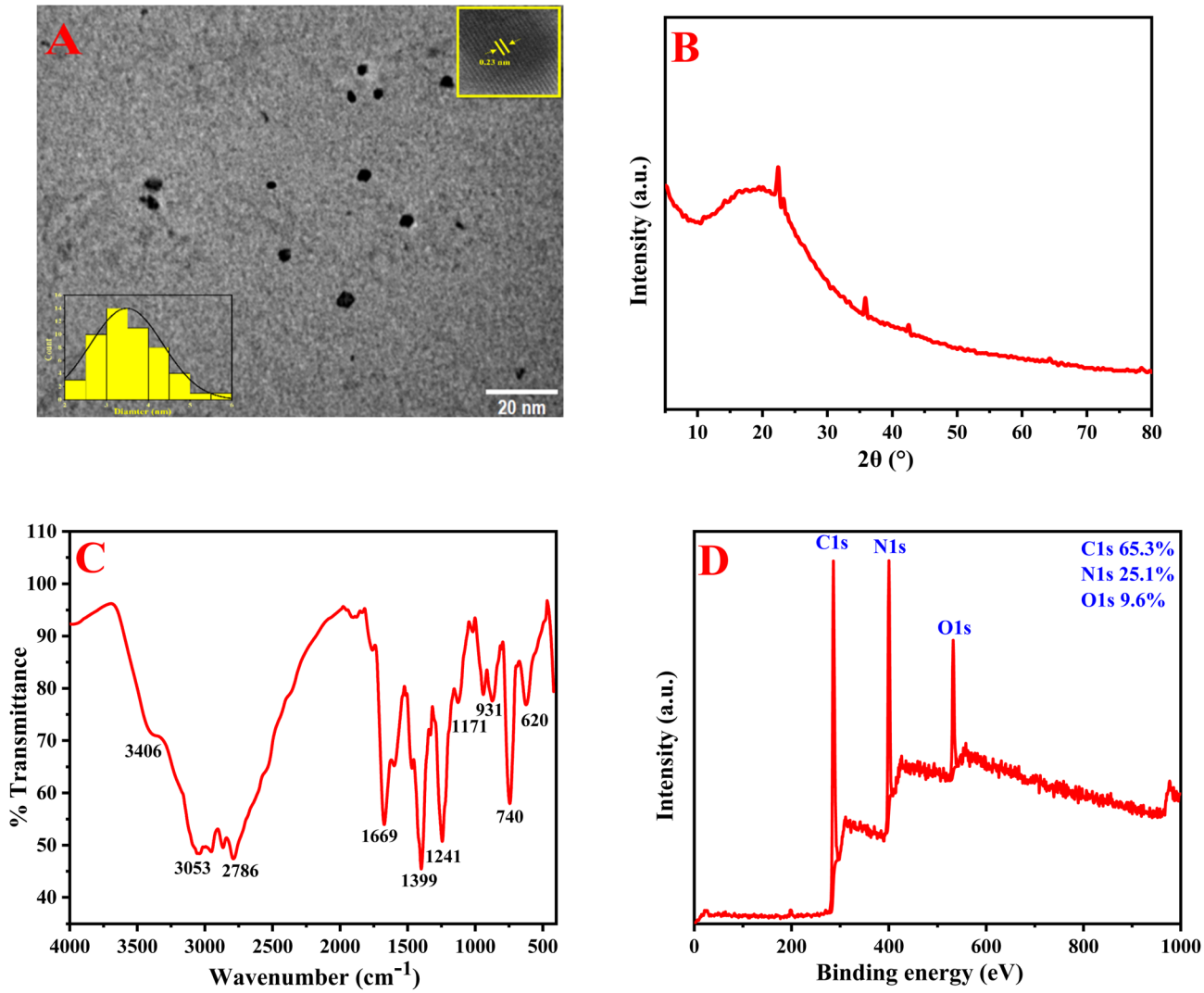

Fig. 1 (A) TEM micrograph; insets show HRTEM image and particle size distribution histogram (B) XRD diffractogram, (C) FT-IR spectra and (D) full XPS survey of O/N-CDs.

water, which is useful for analytical and biological applications.[44]

3.2. UV-vis and fluorescence features of O/N-CDs

The UV-vis spectra of O/N-CDs (Fig. 2A) show two primary absorption peaks. A strong band at 270 nm is caused by $\pi \rightarrow \pi^*$ transitions of sp^2-hybridized carbon in aromatic domains.[41] A weaker band at 385 nm is caused by $n \rightarrow \pi^*$ transitions of C=O and C=N groups. When the dispersion is excited between 260 and 300 nm, it gives off a single wide orange emission band that is centered about 580 nm. The fluorescence intensity is highest when the excitation wavelength is less than 270 nm and slowly drops as the wavelength is changed to longer values. It is very feeble at 300 nm (Fig. 2B). The absolute fluorescence quantum yield is 20.71%, which is in the range that has been reported for OPD-derived carbon dots, where surface molecule states are the main source of emission.[44,46]

3.3. Stability of O/N-CDs

Fluorescence within the pH range of 3.0 to 12.0 was measured to determine the stability of O/N-CDs (Fig. S2A). With increasing pH, the emission intensity peaked at about 8.0 and then began to decrease at higher pH values. The emissive surface and molecular states are modulated by oxygenated surface groups and the protonation and deprotonation of amine and imine sites on phenazine-like molecular emitters.[47] In the pH range of neutral to slightly basic, partial deprotonation increases radiative recombination and reduces non-radiative traps. On the other hand, substantial deprotonation at high pH values promotes non-radiative processes including base-assisted quenching and photoinduced electron transfer.[48] Fig. S2B shows how different NaCl concentrations (0.1–1.3 M) affect O/N-CDs' fluorescence intensity, indicating that O/N-CDs remain stable at high NaCl concentrations. For up to 3.0 hours, the O/N-CDs were exposed to a 365 nm UV lamp in order to assess their resilience. The photostability of the produced O/N-CDs is shown

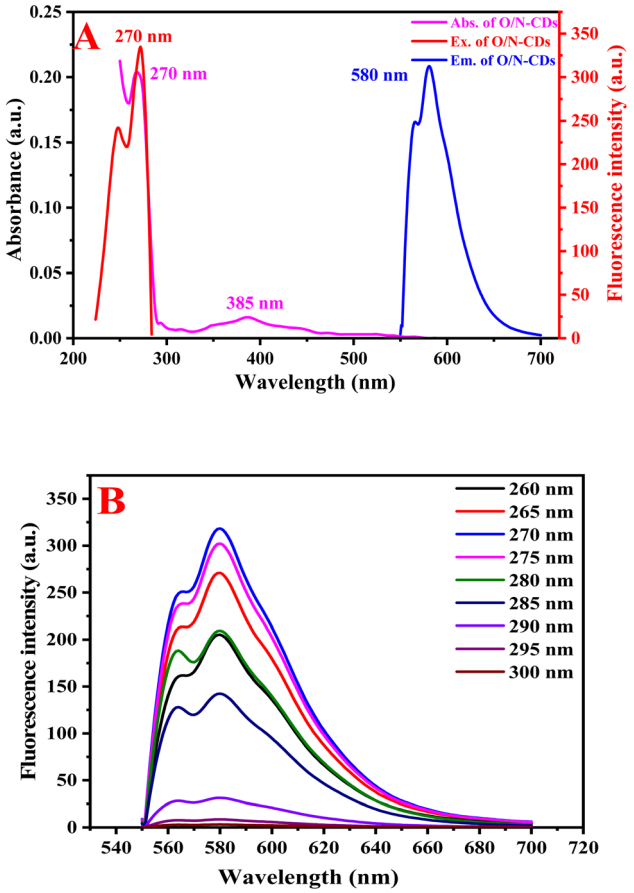

Fig. 2 (A) UV-vis absorption, fluorescence excitation, and emission spectra of the O/N-CDs (12.0 μg mL^{-1}) are presented. (B) The fluorescence emission spectra of O/N-CDs (12.0 μg mL^{-1}) were analyzed using a range of excitation wavelengths (260–300 nm).

in Fig. S2C. Temperature affects O/N-CD fluorescence, which progressively decreases as the temperature rises from 20.0 to 80.0 °C, as seen in Fig. S2D. This quenching is typical of CDs and is indicative of thermally triggered non-radiative decay, where the reduced radiative yield at high temperatures is caused by solvent-assisted collisional quenching and improved excitation–phonon coupling.[48]

3.4. Experimental parameter optimization

To maximize the fluorescence response of the O/N-CDs and ensure robust, reproducible quenching measurements, key experimental variables affecting the emission intensity were optimized, including pH, buffer solution, O/N-CDs volume, and incubation time. The fluorescence intensity of the O/N-CDs was examined over pH 3.0–12.0 using Britton–Robinson universal buffer, which provides broad-range pH control while maintaining a consistent buffer system across the studied pH range. As shown in Fig. S3A, the fluorescence increased with increasing pH and reached a maximum at pH 8.0. This behavior is consistent with the reported pH-sensitive photoluminescence of CDs, where changes in the protonation/deprotonation state of surface functional groups modulate surface states and non-radiative pathways. Therefore, pH 8.0 provides the highest baseline emission and a stable analytical response.[49,50] At pH 8.0, ETX (weak base; reported pK_a = 4.6–5.0) is predominantly in its neutral form, which favors non-covalent association with the O/N-CDs surface *via* hydrogen bonding and hydrophobic/π-interactions, supporting a sensitive and repeatable fluorescence suppression response. Consequently, Britton–Robinson buffer at pH 8.0 was selected for subsequent measurements.[51,52] The volume of the O/N-CDs dispersion was optimized by varying the added volume from 0.2 to 2.0 mL while keeping the final assay volume constant (completed with buffer). As shown in Fig. S3B, 1.2 mL produced the highest and most consistent fluorescence intensity; lower volumes yielded insufficient signal, whereas higher volumes did not improve the response and may introduce concentration-dependent optical effects (*e.g.*, self-absorption/partial self-quenching). Accordingly, 1.2 mL was selected as the optimum volume. Finally, the reaction kinetics were evaluated by monitoring fluorescence immediately after mixing and up to 10.0 min (Fig. S3C). The quenching response was essentially instantaneous and remained stable during the observation period; therefore, an incubation time of 1.0 min was adopted to standardize handling while enabling rapid analysis.

3.5. Analysis of data

A reduction of the O/N-CD fluorescence signal is shown in Fig. 3A, which corresponds to rising ETX concentrations. As shown by the following equation, eight ETX concentration levels (Fig. 3B) were used to illustrate the method's linearity: F_0–F, where F_0 and F represent the probe's fluorescence intensity in the absence and presence of ETX, respectively, is equal to $\Delta F = 0.29\ [\mathrm{ETX}] + 2.29$, $R^2 = 0.9994$. The calibration curve was constructed using eight concentration levels ($n = 8$), with each level measured in triplicate ($n = 3$). Mathematically, the limits of detection (LOD) and quantitation (LOQ) are 3.3 σ/S and 10 σ/S, respectively, where S stands for the slope and σ for the intercept's standard deviation. Table 1 summarizes the parameters and presents them.

The analytical method's accuracy is a crucial validation criterion. In order to determine the percentage recoveries, the fluorescence intensity of three ETX concentration levels (70, 400, and 1000 ng mL^{-1}) was measured six times each using the produced O/N-CDs. The results are displayed in Table S1. By examining three concentration levels six times in a single day and across three days in a row, the method's intra- and inter-day accuracy was evaluated. Relative standard deviations (RSD%) and recovery percentages were calculated and are shown in Table S1. The results show that the suggested strategy is very precise.

3.6. Selectivity

We examined the O/N-CDs sensor's selectivity in detecting ETX under plasma-like conditions. To value the test, we introduced common interferents at purposefully high concentrations while maintaining ETX at 200 ng mL^{-1}. When compared to ETX alone, typical plasma ions such as Na^+, K^+, Ca^{2+}, and Zn^{2+} (as

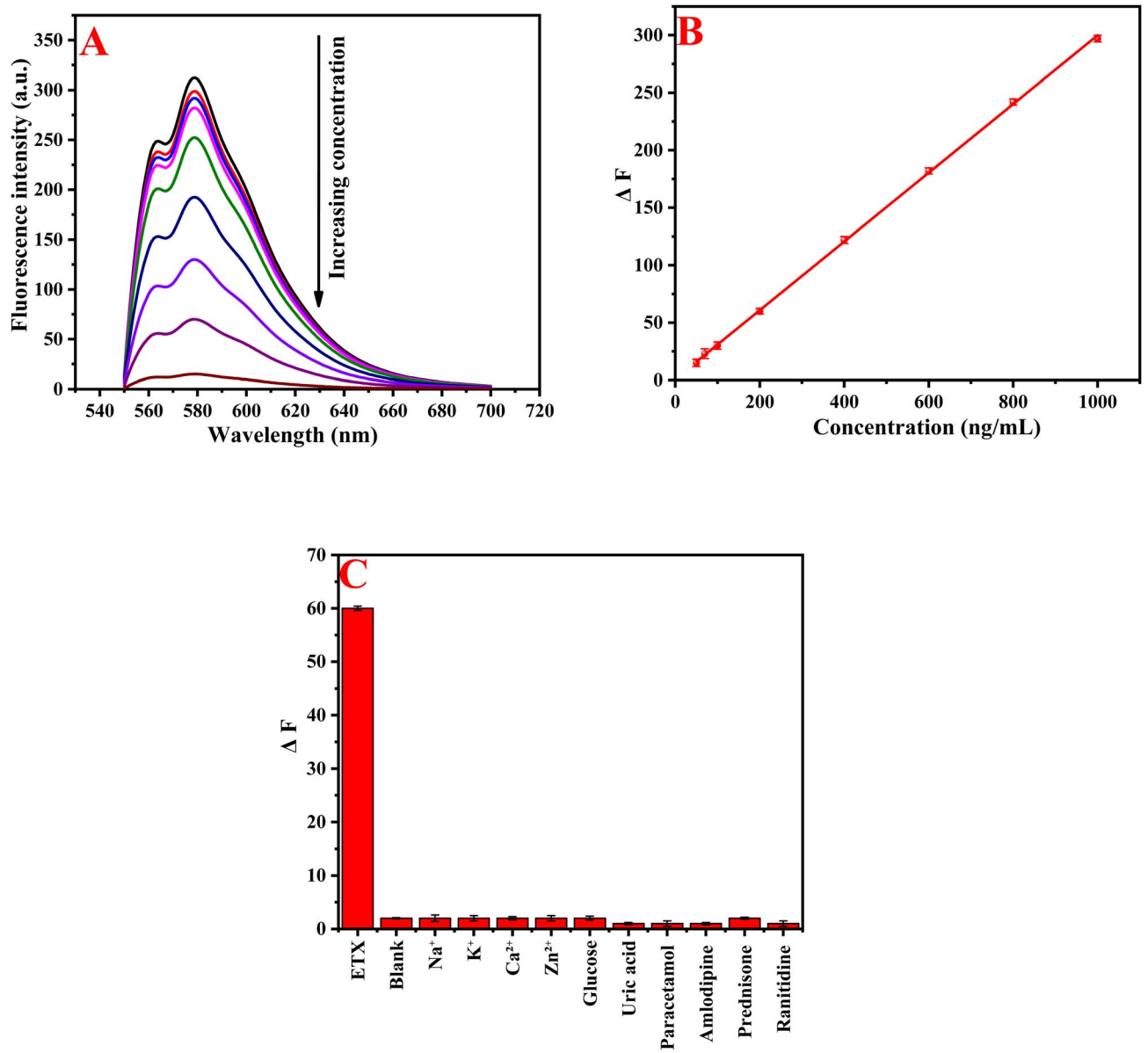

Fig. 3 (A) The impact of different ETX concentrations (0–500 ng mL^{-1}) on the fluorescence emission of O/N-CDs (B) the relationship between Δ*F* and ETX concentration (50–1000 ng mL^{-1}) (C) Effect of ETX (200 ng mL^{-1}) and different (a) endogenous cations (Na^+, K^+, Ca^{2+}, Zn^{2+}) and biological metabolites (glucose, uric acid), (b) potential interfering drugs (paracetamol, prednisone, amlodipine, ranitidine) on the fluorescence quenching (Δ*F*) of O/N-CDs.

Table 1 The quantitative statistical data for determining ETX using the proposed method

Parameter	Values
λ_{ex} (nm)	270
λ_{em} (nm)	580
Linearity range (ng mL^{-1})	50–1000
Intercept ± SD	2.29 ± 1.42
Slope± SD	0.29 ± 0.24
Correlation coefficient (*r*)	0.9996
Coefficient of determination (r^2)	0.9994
LOD (ng mL^{-1})	15.80
LOQ (ng mL^{-1})	47.89

chlorides, 10 mM) did not alter the fluorescence, indicating that the probe can withstand high ionic strength. Additionally, small plasma metabolites such as uric acid (1.0 μg mL^{-1}) and glucose (10 μg mL^{-1}) showed no effect (Fig. 3C). Then, at 3.0 μg mL^{-1}, we employed commonly co-administered medications such as ranitidine, amlodipine, prednisone, and paracetamol. These resulted in little to no additional quenching, suggesting that even with significant co-medication doses, the sensor maintains its selectivity (Fig. 3C). The known sensing mechanism is consistent with this great selectivity. Near 270 nm, ETX exhibits a high overlap with the O/N-CDs excitation band, resulting in a pronounced inner-filter effect (IFE). The signal is further diminished by temperature-dependent dynamic quenching,

which is backed by bigger Stern–Volmer slopes at higher temperatures. The quenching characteristic of ETX cannot be replicated by interferents that do not absorb near 270 nm or that do not interact strongly with the surface states of O/N-CDs. Prior to measurement, we included a basic SPE cleanup to manage matrix effects. The technique produced 94.52–96.01% recoveries in spiking rat plasma and remained linear from 50–1000 ng mL^{-1}, allowing for accurate ETX quantification in complicated samples. These findings demonstrate that the O/N-CDs probe can be selective and regarded as an interference-free measure for ETX at 200 ng mL^{-1} in plasma, in conjunction with the selectivity data previously mentioned (Fig. 3C).

3.7. Proposed quenching pathway

The decrease in fluorescence intensity of O/N-CDs after adding ETX represents fluorescence quenching, which may occur through different mechanisms including inner-filter effect (IFE), fluorescence resonance energy transfer (FRET), and dynamic or static quenching.[53] In the proposed method, increasing ETX concentration produced a gradual reduction in the fluorescence emission of O/N-CDs ($\lambda_{ex} = 270$ nm, $\lambda_{em} = 580$ nm), confirming a concentration-dependent "turn-off" response.

Since ETX exhibits absorption in the excitation region as shown in Fig. 4A, the possibility of IFE was investigated as a starting point for elucidating the mechanism responsible for the recorded fluorescence decrease. The overlap between the UV-vis absorption spectrum of ETX and the excitation band of O/N-CDs indicates that IFE can occur,[54] leading to attenuation of the excitation light reaching the fluorophore. Therefore, the recorded fluorescence intensities were corrected for IFE using:

$$F_{corr} = F_{obs} \times 10^{(A_{ex} + A_{em})/2}$$

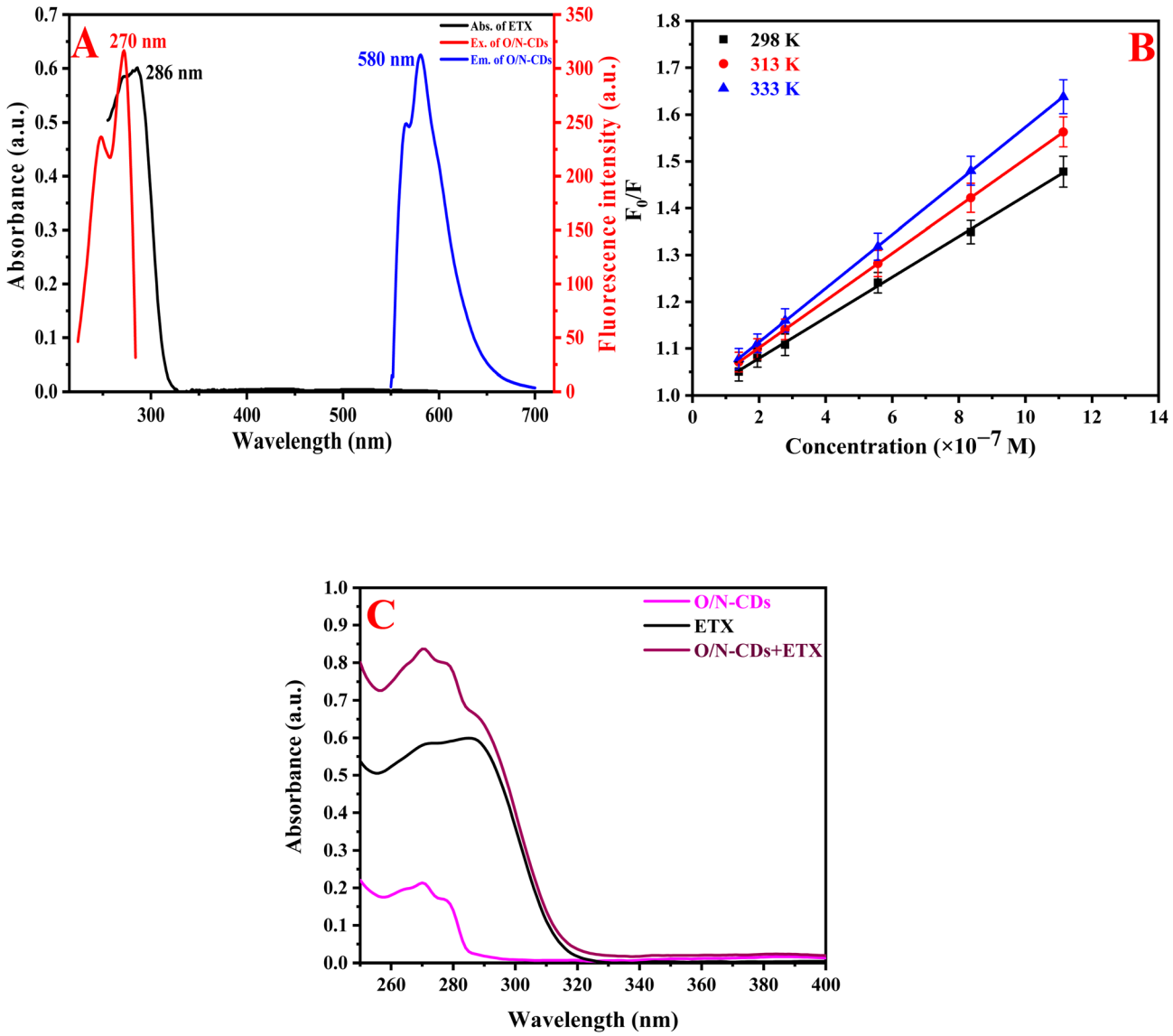

Fig. 4 (A) UV-vis absorption of ETX and excitation/emission spectra of the O/N-CDs, (B) Stern–Volmer plots for the O/N-CDs and ETX mixture at varying temperatures, (C) UV-vis absorption spectra of O/N-CDs, ETX, and their mixtures.

where F_{corr} is the corrected fluorescence intensity after subtraction of IFE from the observed intensity F_{obs}, while A_{ex} and A_{em} are the absorbances of ETX at the excitation and emission wavelengths, respectively. In the proposed method, ETX absorbance at the emission band (580 nm) is negligible; thus, the correction is dominated mainly by A_{ex}.[55]

Next, the suppressed efficiency (%E) was calculated for both the observed and corrected fluorescence intensities according to:

$$E\,(\%) = (1 - F/F_0) \times 100$$

where E (%) is the suppressed efficiency, F represents F_{obs} or F_{corr}, and F_0 is the blank fluorescence intensity of O/N-CDs. As depicted in Fig. S4, subtracting the IFE contribution produced a noticeable decrease in %E, confirming that IFE participates significantly in the overall fluorescence attenuation.[56] Based on the observed *vs.* corrected efficiencies in the 50–400 ng mL^{-1} range, the IFE contribution $\Delta E = E_{obs} - E_{corr}$ corresponds to approximately 39.0–45.8% of the apparent quenching effect. However, an additional mechanism is responsible for the remaining percentage of quenching. Consequently, the Stern–Volmer analysis was utilized to explain the quenching mechanism.[57,58] Aside from (IFE), an alternative mechanism, such as static or dynamic quenching, may also occur.

$$F_0/F = 1 + K_{SV}[Q]$$

where the variable F_0 represents the fluorescence intensity of O/N-CDs. F represents the fluorescence intensity of O/N-CDs after the addition of ETX. K_{SV} is the Stern–Volmer constant, and $[Q]$ is the molar concentration of the drug. Furthermore, graphing F_0/F *versus* $[Q]$ at three different temperatures produced Stern–Volmer graphs (Fig. 4B).

The study revealed an increase in K_{SV} values as the temperature increased, measuring 4.35×10^5 L mol^{-1} at 298 K, 5.04×10^5 L mol^{-1} at 313 K, and 5.74×10^5 L mol^{-1} at 333 K, which suggests the occurrence of dynamic quenching.

Possible static quenching *via* ground-state complex formation was examined by UV-vis spectroscopy (Fig. 4C). The absorption spectrum of the O/N-CDs-ETX mixture matched the arithmetic sum of the individual spectra, with no new bands or measurable bathochromic/hypsochromic shifts, arguing against formation of a stable ground-state complex.[59] Moreover, FRET is unlikely because ETX lacks appreciable absorbance in the donor emission region near 580 nm, and no emission peak shift was observed (Fig. 4A), indicating insufficient spectral overlap for efficient energy transfer.

3.8. Spiked plasma quantification

The proposed spectrofluorometric approach, improved by protein precipitation and subsequent SPE, was validated in spiking rat plasma at concentrations ranging from 50 to 1000 ng mL^{-1}. The calibration exhibited excellent linearity, characterized by the equation: $\Delta F = 0.27\,[\mathrm{ETX}] + 2.53$, with $R^2 = 0.9984$ ($n = 8$), where ΔF signifies the fluorescence change and [ETX] represents the concentration in ng mL^{-1}. The sensitivity parameters were established as follows: limit of detection (LOD) = 16.21 ng mL^{-1} and limit of quantification (LOQ) = 49.11 ng mL^{-1} (Table S2). Extraction experiments revealed mean recoveries of 94.52% and 96.01% (Table 2). The analytical approach employed a 20-fold dilution factor for plasma extracts prior to analysis; this produced a calibration curve covering 50–1000 ng mL^{-1} after dilution each analysis used 250 μL of rat plasma. To check that the method works for real pharmacokinetic samples, we compared it with the reported PK method.[60] Based on the published C_{max} of 6.8 ± 1.2 μg mL^{-1} after 20 mg kg^{-1} oral ETX, scaling to a 12.33 mg kg^{-1} dose gives an estimated C_{max} of about 4.19 μg mL^{-1}. With our sample prep (1 : 1 plasma–methanol dilution, SPE cleanup, then dilution to 5 mL), this corresponds to roughly 210 ng mL^{-1} in the final extract, so the peak levels still fall comfortably within the validated calibration range.

Table 2 Plasma samples were analyzed at four distinct concentrations utilizing the proposed method ($n = 3$)

Added (ng mL^{-1})	Found (ng mL^{-1})	Recovery (%)	RSD (%)
50	47.26	94.52	2.22
100	95.24	95.24	1.27
400	382.68	95.67	2.08
800	768.08	96.01	1.70

3.9. Application of the proposed method to real plasma samples

Following ETX administration, the pharmacokinetic profile was evaluated in two rat groups ($n = 8$/group): a control group with normal hepatic function and a TAA-induced acute liver injury (TAA-ALI) group (Fig. 5). This setup allowed a direct assessment of how acute hepatic impairment influences ETX exposure and disposition (Table 3).

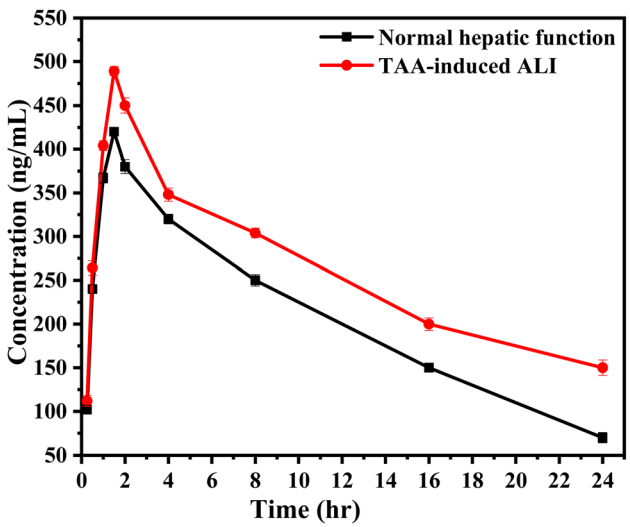

Fig. 5 Mean plasma concentration–time profiles of etoricoxib (ETX) following a single oral dose of 12.33 mg kg^{-1} in rats with normal hepatic function and thioacetamide (TAA)-induced acute liver injury ($n = 8$ per group).

Table 3 Comparison of pharmacokinetic parameters of ETX in control and TAA-ALI rats ($n = 8$)

Parameter	Control group (mean ± SD)	TAA-ALI group (mean ± SD)	p-Value	Significance
K_{el} (1 h^{-1})	0.075 ± 0.002	0.043 ± 0.002	<0.05	Yes
$t_{1/2}$ (h)	9.21 ± 0.17	15.96 ± 0.23	<0.05	Yes
T_{max} (h)	1.52 ± 0.10	1.52 ± 0.10	>0.05	No
C_{max} (ng mL^{-1})	420.46 ± 8.16	489.21 ± 6.36	<0.05	Yes
AUC_{0-t} (ng h mL^{-1})	4044.00 ± 15.6	4804.18 ± 20.4	<0.05	Yes
$AUC_{0-\infty}$ (ng h mL^{-1})	5475.81 ± 25.1	7753.55 ± 24.3	<0.05	Yes
$AUMC_0$ (ng h^2 mL^{-1})	26 939.87 ± 95.7	33 318.38 ± 129.8	<0.05	Yes
$AUMC_0$ (ng h^2 mL^{-1})	83 943.73 ± 272.2	166 802.07 ± 254.8	<0.05	Yes
MRT (h)	15.33 ± 0.16	21.51 ± 0.29	<0.05	Yes
CL/F (L h^{-1} kg^{-1})	0.66 ± 0.02	0.46 ± 0.01	<0.05	Yes
Vd/F (L kg^{-1})	8.80 ± 0.17	8.80 ± 0.17	>0.05	No

In the control group, ETX exhibited rapid absorption, reaching a C_{max} of 420.46 ± 8.16 ng mL^{-1} at a T_{max} of 1.52 ± 0.10 h. Overall exposure was AUC_{0-t} = 4044.00 ± 15.6 ng h mL^{-1} and $AUC_{0-\infty}$ = 5475.81 ± 25.1 ng h mL^{-1}. Moment analysis showed $AUMC_{0-t}$ = 26 939.87 ± 95.7 ng h^2 mL^{-1} and $AUMC_{0-\infty}$ = 83 943.73 ± 272.2 ng h^2 mL^{-1}. Elimination was relatively faster, with K_{el} = 0.075 ± 0.002 h^{-1} and $t_{1/2}$ = 9.21 ± 0.17 h, yielding an MRT of 15.33 ± 0.16 h. Apparent clearance and distribution were CL/F = 0.66 ± 0.02 L h^{-1} kg^{-1} and Vd/F = 8.80 ± 0.17 L kg^{-1} (Table 3).

TAA-induced ALI produced a clear shift in systemic exposure and elimination kinetics while leaving absorption timing and distribution unchanged. T_{max} remained identical (1.52 ± 0.10 h; indicating preserved absorption rate). However, peak exposure increased significantly to C_{max} = 489.21 ± 6.36 ng mL^{-1}. More pronounced differences were seen in extent and persistence of exposure: AUC_{0-t} increased to 4804.18 ± 20.4 ng h mL^{-1} and $AUC_{0-\infty}$ increased to 7753.55 ± 24.3 ng h mL^{-1}. Similarly, $AUMC_{0-t}$ rose to 33 318.38 ± 129.8 ng h^2 mL^{-1} and $AUMC_{0-\infty}$ nearly doubled to 166 802.07 ± 254.8 ng h^2 mL^{-1}, consistent with greater late-time exposure (Table 3).

These exposure changes were accompanied by significantly slower elimination. K_{el} decreased to 0.043 ± 0.002 h^{-1} and $t_{1/2}$ prolonged to 15.96 ± 0.23 h, which increased MRT to 21.51 ± 0.29 h. In parallel, apparent clearance fell markedly to CL/F = 0.46 ± 0.01 L h^{-1} kg^{-1}. In contrast, distribution was not affected: Vd/F remained 8.80 ± 0.17 L kg^{-1} (Table 3). Taken together—unchanged T_{max} and Vd/F, but increased C_{max}, increased AUC/AUMC, decreased CL/F, and prolonged $t_{1/2}$/MRT—the data support impaired hepatic clearance as the primary driver of the altered ETX pharmacokinetics in TAA-ALI rather than changes in absorption rate or tissue distribution.

Mechanistically, this pattern is consistent with ETX being cleared predominantly through hepatic metabolism (with CYP-mediated pathways playing a central role), and with TAA-induced acute liver injury suppressing hepatic drug-metabolizing capacity. Functionally, reduced metabolic clearance would be expected to raise systemic exposure and extend residence time, matching the observed increases in AUC/AUMC and prolongation of half-life and MRT, while leaving distribution largely unchanged (Table 3). Translationally, the findings indicate that acute hepatic dysfunction can significantly increase ETX systemic exposure and prolong its persistence, which may intensify pharmacologic effects and elevate the likelihood of concentration-dependent adverse outcomes. This has direct implications for preclinical safety margin determination and supports the need for dose adjustment strategies and closer monitoring when hepatic function is compromised.

3.10. Comparative analysis with existing approaches

Published methods for ETX determination differ widely in sensitivity, sample-preparation burden, and how easily they translate to biological studies (Table 4). The proposed procedure showed a linear range of 0.05–1.0 μg mL^{-1}, reaching lower concentrations than several HPLC-based bioanalytical assays that commonly start at 0.1 μg mL^{-1} or above. For instance, ultra-performance liquid chromatography with photodiode array detection (UPLC–PDA) has been reported at 0.1–12 μg mL^{-1} in rat plasma,[55] HPLC–DAD at 0.1–10 μg mL^{-1} in human urine,[15] and HPLC–UV at 0.1–50 μg mL^{-1} in human plasma.[16] These chromatographic approaches often require multiple handling steps, including liquid–liquid extraction (LLE) with ethyl acetate, fabric-phase sorptive extraction (FPSE), solvent evaporation, and reconstitution, which increases time and organic-solvent use. LC-MS/MS offers much lower detection capability and can reach sub-ng mL^{-1} levels; one report describes 0.25–600 ng mL^{-1} in rat plasma/brain.[17] That sensitivity comes with practical costs, including expensive instrumentation, trained operators, and method-intensive extraction. In pharmaceutical quality control, several techniques are designed mainly for dosage forms and cover wide concentration ranges, such as HPLC (0.5–85 μg mL^{-1}),[13,14] HPTLC (20–300 and 20–120 μg mL^{-1}),[18,19] UV-vis spectrophotometry (1.5–7.5 μg mL^{-1}),[21] UV spectrophotometry (1.0–40 μg mL^{-1}),[22] and extractive visible spectrophotometry (2.0–18 μg mL^{-1}).[23] Their higher working ranges and the lack of routine validation in biological matrices limit their use in bioanalysis. The proposed spectrofluorometric O/N-CDs method, using protein precipitation followed by SPE, gave recoveries of 94.52% and 96.01% and maintained a bioanalytically relevant range of 0.05–1.0 μg mL^{-1}. The extraction relies on a simplified, largely aqueous SPE approach, with fewer solvent-dependent steps than many non-MS LC approaches. The method was also applied in pharmacokinetic studies in healthy rats and in rats with acute liver

Table 4 Comparative evaluation of the proposed method and published methods

Technique	Sample preparation	Linearity range (μg mL^{-1})	Matrix	Ref.
UPLC-PDA	LLE	0.1–12	Rat plasma	56
HPLC-DAD	FPSE	0.1–10	Human urine	15
HPLC-UV	Protein precipitation	0.1–50	Human plasma	16
LC-MS/MS	LLE with ethyl acetate	0.00025–0.6	Rat plasma/brain	17
RP-HPLC	Dosage form extraction	70–130 (label claim, %)	Tablets	13
RP-HPLC	Dosage form extraction	0.5–85	Tablets	14
HPTLC	Dosage form extraction	20–300	Tablets	18
HPTLC	Dosage form extraction	20–120	Tablets	19
UV-vis and chemometrics	Dosage form extraction	1.5–7.5	Tablets	21
UV spectrophotometry	Dosage form extraction	1.0–40	Tablets	22
Extractive visible spectrophotometry	Dosage form extraction	2.0–18	Tablets	23
Spectrofluorometry (O/N-CDs)	Protein precipitation + SPE	0.05–1.0	Rat plasma	This work

injury, enabling ETX measurement under both normal and impaired hepatic conditions.

3.11. Assessment of greenness and whiteness

To evaluate the sustainability of the proposed spectrofluorometric method, a whiteness assessment was performed consistent with White Analytical Chemistry (WAC) principles, combining the Multi-color Assessment (MA) tool with the Analytical Green Star Area (AGSA) model to capture complementary information on environmental impact, practical applicability, analytical performance, and innovation.[36,37] As detailed in Table 5 and Fig. S5A, the method achieved a final whiteness score of 70.2%, classifying it as a distinctively sustainable procedure. The individual domain scores were calculated as follows: the greenness evaluation metric for analytical methods (GEMAM) at 73.1%, reflecting strong environmental sustainability through reduced solvent toxicity and waste; the blueness applicability grade index (BAGI) at 80.0%, indicating excellent practical feasibility and ease of adoption in routine laboratories; and the redness analytical performance index (RAPI) and violet innovation grade index (VIGI) at 62.5% and 65.0%, respectively, showing moderate analytical performance and innovation.[36] The RAPI evaluation was conducted to ensure consistency with ICH Q2(R1) expectations.[61] Additionally, the complementary AGSA framework yielded a score of 77.27 (Fig. S5B), further confirming the method's strengths in energy efficiency and solvent safety, while identifying sample preparation as an area for future optimization *via* analytical quality by design (AQbD).[37] Collectively, these metrics demonstrate that the proposed approach represents a balanced, user-friendly, and environmentally durable analytical procedure.

3.12. Limitations and challenges

Despite its sub-nanogram sensitivity and fast turnaround, the assay still faces several practical hurdles that users should factor into any inter-laboratory transfer:

- Inner-filter effect (IFE). At high etoricoxib or matrix-chromophore levels the cuvette itself attenuates excitation/emission light, compressing the dynamic range; corrective algorithms or dual-beam optics are needed once absorbance at the excitation wavelength exceeds ≈ 0.2 AU.
- Matrix effects. Plasma proteins and common excipients can either quench or enhance the carbon-dot signal, giving biased results if external-standard calibration is used. Routine validation should therefore include post-extraction spiking or post-column infusion experiments to quantify ion-suppression/-enhancement and, where necessary, adopt matrix-matched or standard-addition calibration.
- Carbon-dot batch variability. Quantum yield and Stern–Volmer constants drift between synthesis batches; each lot should be re-standardised against a reference etoricoxib curve and stored ≤ 4 °C for no more than four weeks.
- Instrument-specific factors. Variations in lamp intensity, slit width and detector gain between fluorimeters can shift baseline F_0; laboratories targeting formal accreditation under ISO/IEC 17025 should bracket every run with a quinine-sulphate control to document system suitability.
- Regulatory expectations. Guidance from the World Health Organization stresses that bioanalytical methods supporting pharmacokinetic or bioequivalence studies must demonstrate robustness across different operators and sites; the items above should therefore appear in the method's risk-assessment and quality-control plan.

Table 5 Quantitative assessment of the method's greenness and whiteness profiles

Assessment tool	Domain/Index	Description	Score obtained
Multi-color assessment (MA)	GEMAM	Green (environmental impact)	73.1%
	BAGI	Blue (practical applicability)	80.0%
	RAPI	Red (analytical performance)	62.5%
	VIGI	Violet (innovation)	65.0%
	Overall	Final whiteness score	70.2%
AGSA model	Total score	Analytical green star area	77.27

4. Conclusion

This work introduces and validates a spectrofluorometric method for etoricoxib (ETX) quantification using orange-emitting oxygen/nitrogen-doped carbon dots (O/N-CDs). The analytical concept relies on a turn-off response driven mainly by the inner filter effect, supported by dynamic quenching, where ETX produces concentration-dependent quenching of O/N-CD fluorescence. Validation data showed strong analytical performance in plasma, with high recovery and low variability, and the use of protein precipitation followed by reversed-phase C_{18} solid-phase extraction improved selectivity by removing endogenous matrix components and reducing interference risk. The method worked well when we applied it to rat pharmacokinetic studies under different physiological conditions. It reliably tracked ETX levels in control rats and, importantly, it clearly picked up disease-related changes in the thioacetamide (TAA)-induced acute liver injury (ALI) group. Compared with controls, rats with ALI showed higher drug exposure (increased AUC), lower apparent clearance, and a longer half-life, while the time to reach the peak concentration changed very little. In addition to its value in preclinical studies, this fluorescence-based assay provides a straightforward and practical alternative to chromatographic methods for routine ETX measurements, especially in labs that do not have mass spectrometry. It can also be extended to translational work, such as comparing pharmacokinetics in hepatic impairment, supporting dose optimization in special populations.

Conflicts of interest

The authors have no conflict of interest to declare.

Data availability

All data supporting the findings of this study are included in this article and its supplementary information (SI). Additional data, if required, can be provided upon reasonable request. Supplementary information is available. See DOI: https://doi.org/10.1039/d6ra00452k.

References

1 A. S. C. Rice, B. H. Smith and F. M. Blyth, *Pain*, 2016, **157**, 791–796.
2 H. Du, S. Li, Z. Tian, J. Lin, L. Li, J. Liu, W. Xiao, L. Dong and X. Zhang, *Sci. Rep.*, 2025, **15**, 35423.
3 J. S. Smolen, D. Aletaha, A. Barton, G. R. Burmester, P. Emery, G. S. Firestein, A. Kavanaugh, I. B. McInnes, D. H. Solomon, V. Strand and K. Yamamoto, *Nat. Rev. Dis. Primers*, 2018, **4**, 18001.
4 A. Rostom, K. Muir, C. Dubé, E. Jolicoeur, M. Boucher, J. Joyce, P. Tugwell and G. W. Wells, *Clin. Gastroenterol. Hepatol.*, 2007, **5**, 818–828.
5 M. Yang, H. T. Wang, M. Zhao, W. B. Meng, J. Q. Ou, J. H. He, B. Zou and P. G. Lei, *Medicine*, 2015, **94**, e1592.
6 A. K. Matsumoto and P. F. Cavanaugh, *Drugs Today*, 2004, **40**, 395–414.
7 S. P. Curtis, B. Bockow, C. Fisher, J. Olaleye, A. Ng, A. Suryawanshi and R. D. Gertz, *BMC Musculoskeletal Disord.*, 2005, **6**, 58.
8 J. K. Takemoto, J. K. Reynolds, C. M. Remsberg, K. R. Vega-Villa and N. M. Davies, *Clin. Pharmacokinet.*, 2008, **47**, 703–720.
9 N. G. B. Agrawal, M. J. Rose, C. Z. Matthews, E. J. Woolf, A. G. Porras, L. A. Geer, P. J. Larson, J. Cote, S. C. Dilzer, K. C. Lasseter, I. Alam, K. J. Petty and K. M. Gottesdiener, *J. Clin. Pharmacol.*, 2003, **43**, 1136–1148.
10 N. V. S. Ramakrishna, K. N. Vishwottam, S. Wishu and M. Koteshwara, *J. Chromatogr. B*, 2005, **816**, 215–221.
11 A. K. Shakya and N. A. Khalaf, *Asian J. Chem.*, 2007, **19**, 5241–5250.
12 U. Mandal, D. S. Rajan, A. Bose, K. V. Gowda, A. Ghosh and T. K. Pal, *Indian J. Pharm. Sci.*, 2006, **68**, 485–489.
13 B. Singh, R. Santhakumar, I. Bala, S. B. Prasad and S. Verma, *Int. J. Pharm. Qual. Assur.*, 2015, **6**, 1–7.
14 S. Topalli, T. G. Chandrasekhar and M. M. Annapurna, *J. Chem.*, 2012, **9**, 832–838.
15 A. Korpeti, N. Manousi, A. Kabir, C. K. Zacharis and E. Rosenberg, *Separations*, 2025, **12**, 141.
16 V. V. P. Pavan Kumar, M. C. A. Vinu, A. V. Ramani, R. Mullangi and N. R. Srinivas, *Biomed. Chromatogr.*, 2006, **20**, 125–132.
17 W. D. Eure, R. G. Grossman, P. J. Horner and D. S.-L. Chow, *Talanta Open*, 2021, **4**, 100052.
18 G. Maheshwari, G. S. Subramanian, A. Karthik, A. Ranjithkumar, P. Musmade, P. M. K. Ginjupalli and N. Udupa, *J. Planar Chromatogr.–Mod. TLC*, 2007, **20**, 335–339.
19 N. J. Shah, S. J. Shah, D. M. Patel and N. M. Patel, *Indian J. Pharm. Sci.*, 2006, **68**, 788–789.
20 S. Singh, A. Mishra, A. Verma, A. K. Ghosh and A. K. Mishra, *J. Adv. Pharm. Technol. Res.*, 2012, **3**, 237–240.
21 M. A. A. Rahman, M. R. Elghobashy, H. E. Zaazaa and S. S. El-Mosallamy, *BMC Chem.*, 2023, **17**, 176.
22 M. K. Thimmaraju, V. Rao, K. Hemanth and K. Siddartha, *Int. J. PharmTech Res.*, 2012, **4**, 860–865.
23 K. Shah, A. Gupta and P. Mishra, *J. Chem.*, 2009, **6**, 207–212.
24 S. L. Dalmora, M. da Silva Sangoi, L. M. da Silva, R. O. Macedo and T. Barth, *J. Sep. Sci.*, 2008, **31**, 169–176.
25 A. Truskewycz, H. Yin, N. Halberg, D. T. H. Lai, A. S. Ball, V. K. Truong, A. M. Rybicka and I. Cole, *Small*, 2022, **18**, 2106342.
26 S. R. Lodha, J. G. Merchant, A. J. Pillai, A. H. Gore, P. O. Patil, S. N. Nangare, G. G. Kalyankar, S. A. Shah, D. R. Shah and S. P. Patole, *Heliyon*, 2024, **10**, e41020.
27 M. Elnaggar, H. Elbardisy, A. El-Yazbi and T. S. Belal, *J. Adv. Pharm. Sci.*, 2024, **1**, 42–59.
28 B. I. Salman, M. A. Abdel-Lateef, E. Alzahrani, A. Al-Harrasi, A. E. Ibrahim, E. A. M. El-Shoura and Y. F. Hassan, *Luminescence*, 2024, **39**, e4801.

29 S. I. Alaqel, O. Abdullah, A. Alharbi, Y. S. Althobaiti, M. S. Alturki, S. Ramzy and A. H. Almalki, *RSC Adv.*, 2023, **13**, 17765–17774.
30 R. Ding, Y. Chen, Q. Wang, Z. Wu, X. Zhang, B. Li and L. Lin, *J. Pharm. Anal.*, 2022, **12**, 355–364.
31 F. Du, R. Chen, E. Feng, H. Dai and F. Yu, *Coord. Chem. Rev.*, 2026, **551**, 217460.
32 Y. Tao, C. Liao, F. He, Y. He and L. Wang, *Food Chem.*, 2025, **487**, 144754.
33 C. Zhao, P. Yuan, D. Wang and D. Fang, *Food Chem.*, 2024, **441**, 138284.
34 W. Yang, C. Wu, N. Wang, G. Song, X. Ni and W. Huang, *J. Inorg. Organomet. Polym. Mater.*, 2021, **31**, 4177–4187.
35 S. L. Dalmora, L. Brum Junior, R. M. Ferretto, P. R. de Oliveira, T. Barth and M. da S. Sangoi, *Quim. Nova*, 2008, **31**, 574–578.
36 A. E. F. Abbas, O. Al Kamaly, G. Magdy and M. K. Halim, *Microchem. J.*, 2025, **216**, 114781.
37 F. R. Mansour, A. Bedair, F. Belal, G. Magdy and M. Locatelli, *Sustainable Chem. Pharm.*, 2025, **46**, 102051.
38 H. Zhi, Y. Dai, L. Su, L. Yang, W. Wu, Z. Wang, X. Zhu, L. Liu, J. Aa and H. Yang, *Biomedicines*, 2023, **11**, 3314.
39 R. Bruck, H. Aeed, Y. Avni, H. Shirin, Z. Matas, M. Shahmurov, I. Avinoach, G. Zozulya, N. Weizman and A. Hochman, *J. Hepatol.*, 2004, **40**, 86–93.
40 S. Reagan-Shaw, M. Nihal and N. Ahmad, *FASEB J.*, 2008, **22**, 659–661.
41 Y. Zhang, M. Huo, J. Zhou and S. Xie, *Comput. Methods Programs Biomed.*, 2010, **99**, 306–314.
42 H. Barhum, T. Alon, M. Attrash, A. Machnev, I. Shishkin and P. Ginzburg, *ACS Appl. Nano Mater.*, 2021, **4**, 9919–9931.
43 C. Ji, Q. Han, Y. Zhou, J. Wu, W. Shi, L. Gao, R. M. Leblanc and Z. Peng, *Carbon*, 2022, **192**, 198–208.
44 Q. Zhang, S. Xu, L. Zhang, L. Yang and C. Jiang, *Adv. Sci.*, 2024, **11**, 2400781.
45 G. Karakus, *Appl. Nanosci.*, 2023, **13**, 6667–6696.
46 T. Li, S. E, J. Wang and X. Chen, *Anal. Chim. Acta*, 2019, **1088**, 107–115.
47 K. Chang, Q. Zhu, L. Qi, M. Guo, W. Gao and Q. Gao, *Materials*, 2022, **15**, 466.
48 Y. Song, S. Zhu, S. Xiang, X. Zhao, J. Zhang, H. Zhang, Y. Fu and B. Yang, *Nanoscale*, 2014, **6**, 4676–4682.
49 M. Alzweiri, M. Sallam, W. Al-Zyoud and K. Aiedeh, *Symmetry*, 2018, **10**, 288.
50 L. Guo, L. Li, X. Wang, Y. Zhang and F. Cui, *ACS Omega*, 2023, **8**, 37098–37107.
51 C. Liu, F. Zhang, J. Hu, W. Gao and M. Zhang, *Front. Chem.*, 2021, **8**, 605028.
52 A. O. da Silva, M. O. Rodrigues, M. H. Sousa and A. F. C. Campos, *Colloids Surf., A*, 2021, **621**, 126578.
53 M. R. Eftink and C. A. Ghiron, *Anal. Biochem.*, 1981, **114**, 199–227.
54 S. K. Panigrahi and A. K. Mishra, *J. Photochem. Photobiol., C*, 2019, **41**, 100318.
55 C. A. Parker and W. T. Rees, *Analyst*, 1960, **85**, 587–600.
56 A. V. Fonin, A. I. Sulatskaya, I. M. Kuznetsova and K. K. Turoverov, *PLoS One*, 2014, **9**, e103878.
57 M. H. Gehlen, *J. Photochem. Photobiol., C*, 2020, **42**, 100338.
58 J. R. Lakowicz and G. Weber, *Biochemistry*, 1973, **12**, 4161–4170.
59 H. Sahoo, *J. Photochem. Photobiol., C*, 2011, **12**, 20–30.
60 S. Ifrah, D. Porat, M. Deutsch and A. Dahan, *Pharmaceuticals*, 2024, **17**, 507.
61 ICH Harmonised Tripartite Guideline, *Validation of Analytical Procedures: Text and Methodology*, Q2(R1), 2005.